Breathing chromium spinels: a showcase for a variety of pyrochlore Heisenberg Hamiltonians – Supplementary Information –

Pratyay Ghosh,[1] Yasir Iqbal,[1] Tobias Müller,[2] Ravi T. Ponnaganti,[1] Ronny Thomale,[2] Rajesh Narayanan,[1] Johannes Reuther,[3,4] Michel J. P. Gingras,[5,6] and Harald O. Jeschke[7]

[1] *Department of Physics, Indian Institute of Technology Madras, Chennai 600036, India*
[2] *Institute for Theoretical Physics and Astrophysics, Julius-Maximilians-Universität Würzburg, Am Hubland, 97074 Würzburg, Germany*
[3] *Dahlem Center for Complex Quantum Systems and Fachbereich Physik, Freie Universität Berlin, 14195 Berlin, Germany*
[4] *Helmholtz-Zentrum für Materialien und Energie, Hahn-Meitner-Platz 1, 14109 Berlin, Germany*
[5] *Department of Physics and Astronomy, University of Waterloo, Waterloo, Ontario, N2L 3G1, Canada*
[6] *Quantum Materials Program, Canadian Institute for Advanced Research, MaRS Centre, West Tower 661 University Ave., Suite 505, Toronto, ON, M5G 1M1, Canada*
[7] *Research Institute for Interdisciplinary Science, Okayama University, Okayama 700-8530, Japan*

(Dated: November 23, 2019)

Supplementary Note 1. Additional DFT details

We show the result of the energy mapping for the two low temperature structures of $LiInCr_4O_8$[1] and $LiGaCr_4S_8$[2] in Supplementary Figure 1.

The energy mapping scheme[3,4] for the chromium breathing pyrochlores works very well. Total moments are exact multiples of 3 μ_B as all chromium moments are exactly $S = 3/2$. All fits are extremely good, with an example given in Supplementary Figure 2.

For convenience, we show in Supplementary Table 1 the average nearest-neighbor energy scale $\bar{J} = \sqrt{J^2 + J'^2}$ for all compounds and all (room temperature and low temperature) structures on record as discussed in the main text (see Table 1).

It is an important finding that the breathing anisotropy found in the exchange couplings is not simply connected to the structural breathing anisotropy. To facilitate the comparison, we list in Supplementary Table 2 the two Cr-Cr distances within small and large tetrahedra for the six room temperature and the two low temperature structures.

It is known that the paramagnetic Curie law in pyrochlores may only be reached at rather high temperatures, leading to possible inaccuracies in experimentally determined Curie-Weiss temperatures[5]. In the case of the breathing pyrochlores, the Curie-Weiss fits were done in a 200 K to 350 K range for $LiInCr_4O_8$ and $LiGaCr_4O_8$[6], in a 200 K to 300 K range for $LiInCr_4S_8$, $LiGaCr_4S_8$ and $CuInCr_4S_8$[7] and using temperatures up to 380 K for $CuInCr_4Se_8$[8]. Note that the conclusions of this work will not change even if a 10% or 20% underestimation of the Curie-Weiss temperatures would force us to revise down the U values at which we read off the relevant model Hamiltonians in Figure 2 of the main text. For the oxides, the Hamiltonian will remain in the same limit even if U is lowered substantially. The same is true for the sulfides because the FM coupling of the large tetrahedron does not depend much on U.

Supplementary Note 2. Additional PFFRG data

In the pseudo-Fermion functional renormalization group (PFFRG) approach, the onset of magnetic long-range order is signaled by a breakdown of the smooth renormalization group (RG) flow. Figure 3 shows the flows computed for the room temperature structures of all six breathing pyrochlore compounds considered in this study. The continuation of the flow below the breakdown energy scale is shown with a dashed line as the PFFRG calculation becomes less reliable in the ordered state. The ordering temperatures determined in this way are the following: $LiInCr_4O_8$ orders at 60.6 K with ordering wave vector $\mathbf{q} = (2, 1, 0)$ (experiment $T_N = 15.9$ K[6]). $LiGaCr_4O_8$ orders at 159.8 K with ordering wave vector $\mathbf{q} = (2, 1, 0)$ (experiment $T_N = 13.8$ K[6]). $LiInCr_4S_8$ orders at 95.0 K with ordering wave vector $\mathbf{q} = (1, 0, 0)$ (experiment $T_c = 24$ K[7]). $LiGaCr_4S_8$ orders at 49.1 K with ordering wave vector $\mathbf{q} = (1, 0, 0)$ (experiment $T_c = 10$ K[2,7]). $CuInCr_4S_8$ orders at 114.7 K with ordering wave vector $\mathbf{q} = (1, 0, 0)$ (experiment $T_c = 40$ K[9], $T_c = 35$ K[10], $T_c = 32$ K[7]. $CuInCr_4Se_8$ orders at 99.3 K with ordering wave vector $\mathbf{q} = (0.521, 0, 0)$ (experiment $T_c = 14$ K[11]).

Oxides.- The room temperature susceptibility profiles of $LiInCr_4O_8$ are shown in the main text (see Figures 3**a-b**). The PFFRG calculation with the low temperature structure of $LiInCr_4O_8$ yields the susceptibility profiles shown in figure 4**a-b** which is calculated with the $T = 20$ K Hamiltonian parameters from Table 1 of the main text. Even though the breathing anisotropy is reduced from $J'/J = 0.37$ to $J'/J = 1$, the two static spin susceptibility profiles are very similar.

Concerning the disagreement of both PFFRG and classical Monte Carlo[13] calculations with the experimental $T = 150$ K neutron data, we speculate that a possible suppression of magnetic scattering at low angles due to the strong neutron absorption of In might explain this discrepancy and would be worth further investigat-

Supplementary Table 1. **Overview of subleading exchange couplings.** Longer range exchange couplings of the chromium breathing pyrochlore compounds are given relative to the average nearest-neighbor energy scale $\bar{J} = \sqrt{J^2 + J'^2}$. The absolute numbers are provided in Table 1 of the main text.

Material	T (K)	$\bar{J}$ (K)	$J_2/\bar{J}$	$J_{3a}/\bar{J}$	$J_{3b}/\bar{J}$	$(J_2 - J_{3a})/\bar{J}$
$LiInCr_4O_8$	20	57.5	0.006	0.035	0.016	−0.030
$LiInCr_4O_8$	RT	63.7	0.004	0.029	0.015	−0.025
$LiGaCr_4O_8$	RT	120.0	0.006	0.016	0.011	−0.011
$LiInCr_4S_8$	RT	27.8	0.025	0.190	0.086	−0.165
$LiGaCr_4S_8$	10	14.3	0.083	0.432	0.215	−0.350
$LiGaCr_4S_8$	RT	14.4	0.081	0.422	0.210	−0.341
$CuInCr_4S_8$	RT	29.6	0.038	0.215	0.153	−0.177
$CuInCr_4Se_8$	RT	40.1	0.008	0.117	0.094	−0.109

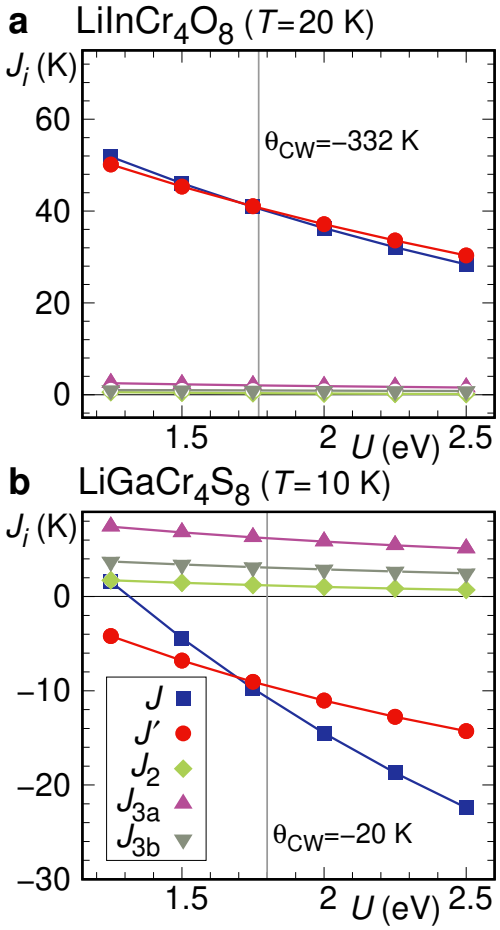

Supplementary Figure 1. **Exchange couplings of two breathing chromium spinels.** The values are calculated by mapping of DFT total energies for low temperature structures of **a** $LiInCr_4O_8$[1] and **b** $LiGaCr_4S_8$[2]. Couplings are shown as a function of the interaction strength U. Vertical lines indicate the U value at which the experimental Curie-Weiss temperature is realized. The $T = 20$ K internal coordinates of $LiInCr_4O_8$ were privately communicated by Goran Nilsen.

ing, for example by performing the same experiment on $LiGaCr_4O_8$ (Ga has a 70 times smaller neutron absorption cross section than In[12]). Another possible explana-

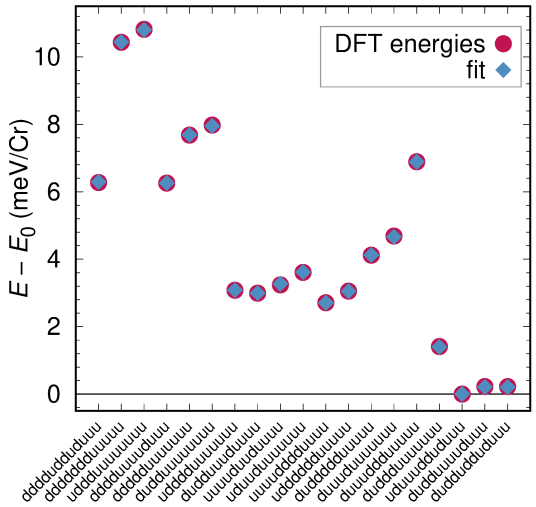

Supplementary Figure 2. **Quality of the energy mapping scheme.** Density functional theory energies for 19 different spin configurations of $LiInCr_4O_8$ calculated with GGA+U exchange correlation functional at $U = 2$ eV and $J_H = 0.72$ eV. The fit to the Heisenberg Hamiltonian with six exchange couplings is excellent.

tion involves the inelasticity of scattering at high tem-

Supplementary Table 2. **Structural breathing anisotropy.** The two smallest Cr^{3+}–Cr^{3+} distances r and r' for the investigated breathing pyrochlores are listed together with the (lattice) breathing anisotropy r'/r. RT stands for room temperature.

Material	T (K)	$r \equiv d^J_{Cr-Cr}$ (Å)	$r' \equiv d^{J'}_{Cr-Cr}$ (Å)	r'/r
$LiInCr_4O_8$[1]	20	2.929	3.014	1.029
$LiInCr_4O_8$[6]	RT	2.903	3.051	1.051
$LiGaCr_4O_8$[6]	RT	2.867	2.970	1.036
$LiInCr_4S_8$[7]	RT	3.429	3.735	1.089
$LiGaCr_4S_8$[2]	10	3.404	3.641	1.070
$LiGaCr_4S_8$[7]	RT	3.397	3.649	1.074
$CuInCr_4S_8$[7]	RT	3.405	3.709	1.089
$CuInCr_4Se_8$[17]	RT	3.613	3.864	1.070

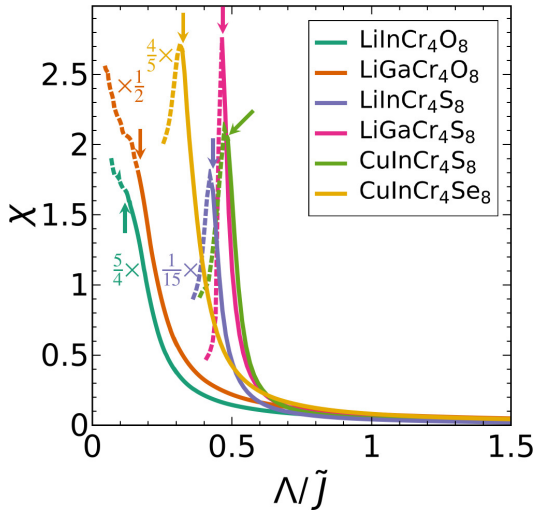

Supplementary Figure 3. **Detection of magnetic order.** RG flows of the maximum of magnetic susceptibilities of all the six compounds under investigation. The points at which the solid lines become dashed indicate an instability in the flow and express the onset of a magnetic order.

peratures which could explain a shift of spectral weight to low Q.

Sulfides.- The spin susceptibility profile of $LiGaCr_4S_8$ is shown in the main text (see Figure 3**g-i**). The other two sulfide spin susceptibility profiles are shown in Supplementary Figures 4**d-e** and **g-h**. All three sulfide PFFRG results are rather similar even though the Hamiltonians do not appear so similar at the outset. As explained in the main text, this can be understood by recognizing that the ferromagnetic large tetrahedra form an fcc lattice of large $S = 6$ magnetic moments, as illustrated in Supplementary Figure 5**a**. The renormalized nearest-neighbor interaction in the fcc lattice is given by $J_1^{\text{fcc}} = (J + 4J_2 + 2J_{3a} + 2J_{3b})/16$ as can be read off from Supplementary Figure 5**b**. For the three sulfides, J_1^{fcc} turns out to be antiferromagnetic.

In the main text, we show that the form factor modulated powder averaged susceptibility $|F(Q)|^2 S(Q)$ which we calculated for $CuInCr_4S_8$ matches the experimental data of Refs.[9,10] very well, accurately reproducing three peak positions at $T = 85$ K (see Figure 5**d** of the main text). We wish to investigate the question to what extent the subleading exchange couplings are important for this very good agreement. To do so, we calculate $|F(Q)|^2 S(Q)$ for Hamiltonians where we set selected longer range couplings to zero; we consider the set J-J'-J_2 (J_{3a} and J_{3b} are neglected), the set J-J'-J_2-J_{3a} (J_{3b} is neglected) and the set J-J'-J_2-J_{3b} (J_{3a} is neglected). The results are shown in Supplementary Figure 6. From both plots, it's clear that the best match with the experimental data is obtained only with the full J-J'-J_2-J_{3a}-J_{3b} model. Each omission of a subleading coupling leads to a worse match with experiment. This validates the values we determined for $CuInCr_4S_8$ using DFT energy mapping and underlines the crucial role played by the subleading couplings up to third nearest neighbor in the breathing pyrochlores.

Supplementary Note 3. Luttinger-Tisza calculations

We employ the Luttinger-Tisza method[14–16] to better understand the classical ground states of the breathing pyrochlore Hamiltonians. Supplementary Figure 7 shows the evolution of the eigenvalues of the Luttinger-Tisza matrix for various breathing anisotropies J'/J. The minimum of the resulting bands identifies the ordering vector of the classical Hamiltonian in reciprocal space. The minima can also be degenerate, and the method allows us to identify one-, two- or even three-dimensional classical degeneracies of the ground state manifold.

Relevant for the chromium oxide spinels, Supplementary Figures 7**a** to **d** show the eigenvalues for antiferromagnetic J and J'. The lowest Luttinger-Tisza band is completely flat, indicating a three-dimensional manifold of degenerate ground states. Decreasing J as compared to J' in Supplementary Figures 7**b**, **c** and **d** only shrinks the band width but does not lift the degeneracy of the lowest band. This explains why the typical bow-tie pattern in the magnetic susceptibility is nearly independent of the J'/J ratio.

For a better understanding of the chromium sulfide spinels, Supplementary Figures 7**e** to **h** show the case of a ferromagnetic large tetrahedron J' together with several antiferromagnetic J values. In this case, the minima of the lowest Luttinger-Tisza band correspond to the lines marked in red, with the ground state displaying a one-dimensional sub-extensive degeneracy. Again, this degeneracy is independent of the value of the J'/J ratio. This explains why the three sulfides show very similar susceptibilities even though their Hamiltonians are rather distinct.

Supplementary Note 4. Classical Monte Carlo results

Supplementary Figure 8 shows the static spin structure factor as obtained from classical Monte Carlo simulations for $CuInCr_4Se_8$ at six different temperatures. In the vicinity of the ordering temperature $T/\bar{J} = 0.20$ the spectral weight is distributed in a nonuniform fashion being concentrated around the Bragg peaks of the incipient incommensurate spiral order. With increasing temperatures, the overall intensity of $S(\mathbf{q})$ decreases but the distribution of spectral weight becomes progressively homogeneous over a ring-like shape in the $[hk0]$ and $[hhl]$ planes. At temperatures of $\sim 1.5T_{\text{ord}}$ we observe (i) a near uniform distribution of $S(\mathbf{q})$ along a ring-like shape, (ii) a concentrated distribution of $S(\mathbf{q})$ in a ring-like pattern of small width, and (iii) well-separated spiral rings.

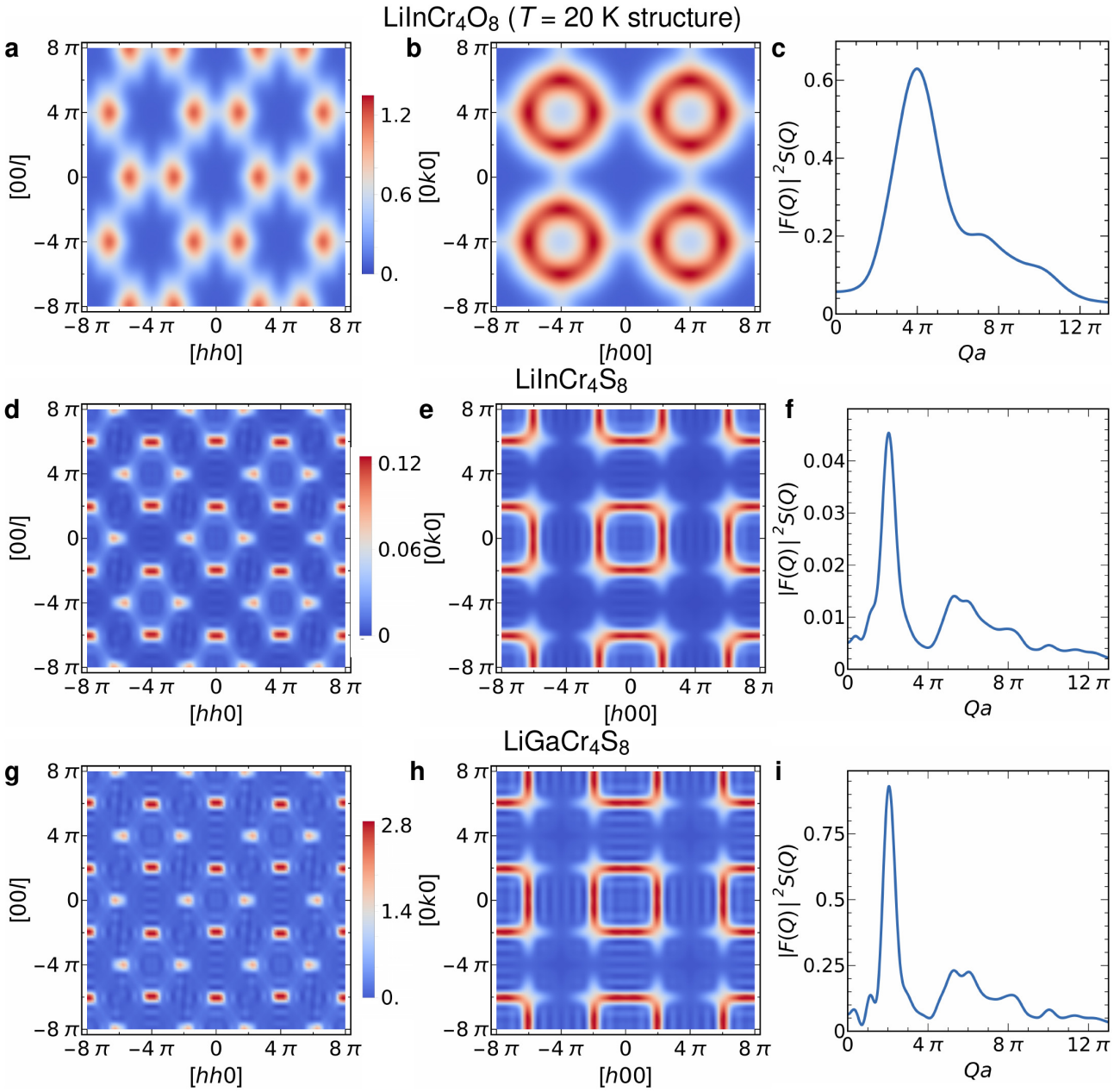

Supplementary Figure 4. **Additional spin susceptibility profiles.** PFFRG results for the $T = 20$ K Hamiltonian of $LiInCr_4O_8$, for $LiInCr_4S_8$ and for $LiGaCr_4S_8$ are shown. They are evaluated at the breakdown point in the RG flow, marked by an arrow in Supplementary Figure 3. **a**, **d**, **g** Spin susceptibility projected on the $[hhl]$ plane. **b**, **e**, **h** Spin susceptibility projected on the $[hk0]$ plane. Susceptibility units are $1/\bar{J}$ ($\bar{J} = \sqrt{J^2 + J'^2}$), and the axes are in units of inverse lattice parameter $1/a$. **c**, **f**, **i** Plots of the form factor modulated powder averaged susceptibility $|F(Q)|^2 S(Q)$ vs. Qa.

The existence of these features points to the appearance of a temperature regime hosting an approximate spiral spin liquid.

Supplementary Note 5. Basis effects in the structure factor

We investigate the origin of the calculated susceptibilities of the chromium sulfides shown in Figures 3**g-h** of the main text and Supplementary Figures 4**d-e** and **g-h**. For this purpose, we use the Luttinger-Tisza method[14–16] to calculate the structure factor of the antiferromagnetic Heisenberg Hamiltonian on the fcc lattice. The result is

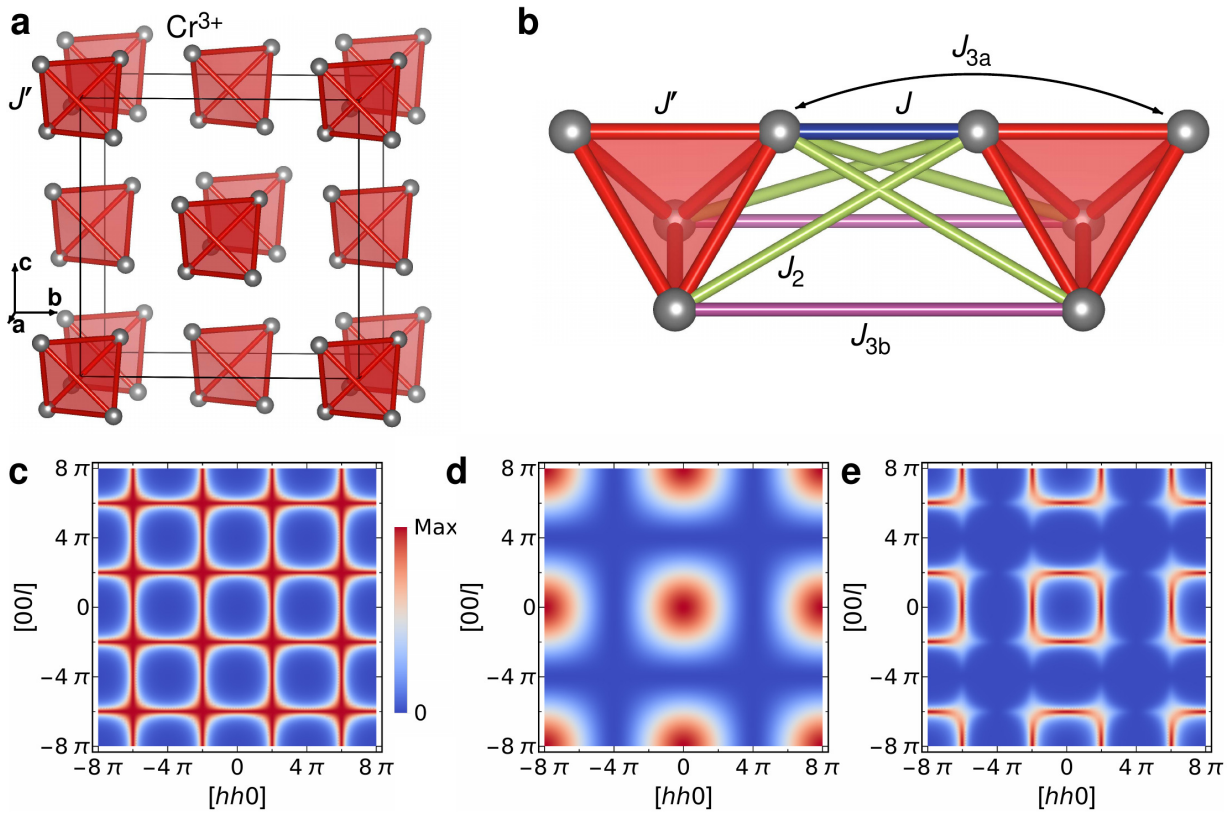

Supplementary Figure 5. **Consequences of the effective fcc lattice. a** Large tetrahedra of the chromium sulfides, forming an fcc lattice. Only the strong ferromagnetic J' coupling is depicted which turns the Cr^{3+} tetrahedra into approximate $S = 6$ units. **b** Exchange interactions between nearest-neighbor large tetrahedra in the fcc structure. **c** Classical spin susceptibility from Luttinger-Tisza of the fcc nearest-neighbor Heisenberg antiferromagnet (NNAF) just above the ordering temperature; the critical temperature of the NNAF on the fcc lattice is $T_c = \frac{4}{3}J$, the plot is done at $T = 1.48J$. **d** Structure factor $|f(\mathbf{q})|^2$ of the pyrochlore basis. **e** Classical spin susceptibility of a effective fcc nearest-neighbor model on the pyrochlore lattice formed by ferromagnetically ordered tetrahedra in **a**, given by the product of **c** and **d**.

shown in Supplementary Figure 5**c**. Now, we have to take into account the fact that the classical $S = 6$ magnetic moment on the fcc lattice is not point-like but instead has an internal structure – the moment being composed of six $S = 3/2$ moments arranged on a tetrahedron constituting a basis. Thus, the complete structure factor of the pyrochlore lattice is now determined by multiplying the spin structure factor on the fcc lattice with the square of the absolute value of the Fourier transform of the magnetic basis

$$f(\mathbf{q}) = \frac{1}{4}\left(1 + e^{-i\frac{a}{4}(q_x+q_y)} + e^{-i\frac{a}{4}(q_x+q_z)} + e^{-i\frac{a}{4}(q_y+q_z)}\right). \tag{1}$$

The susceptibility profiles therefore acquire a factor of $|f(\mathbf{q})|^2$ between fcc and pyrochlore lattice:

$$S_{\text{Pyro}}(\mathbf{q}) = |f(\mathbf{q})|^2 S_{\text{fcc}}(\mathbf{q}). \tag{2}$$

The classical spin susceptibility of a fcc nearest-neighbor Heisenberg antiferromagnet, relevant to the sulfides consists of degenerate maxima in the $[hk0]$ planes along the lines $\mathbf{q} = \frac{2\pi}{a}(\pm n, \delta, 0)$ and $\mathbf{q} = \frac{2\pi}{a}(\delta, \pm n, 0)$, which form edge sharing squares with side length $4\pi/a$ in reciprocal space, as shown in Supplementary Figure 5**c**. The factor $|f(\mathbf{q})|^2$, shown in Supplementary Figure 5**d** is 1 at $(0, 0, 0)$, and zero on the lines $\mathbf{q} = \frac{4\pi}{a}(\pm n, \delta, 0)$ and $\mathbf{q} = \frac{4\pi}{a}(\delta, \pm n, 0)$, and thus 8π periodic. This implies that every second row and column of squares in the fcc susceptibility is suppressed by the sublattice structure (see Supplementary Figure 5**e**), this giving rise to a pattern of disconnected squares of maxima on the pyrochlore lattice which are also modulated in their intensity. Indeed, this is precisely what PFFRG finds for the chromium sulfide breathing pyrochlores (see Figures 3**g**-**h** of the main text and Supplementary Figures 4**d**-**e** and **g**-**h**).

[1] Nilsen, G. J. et al. Complex magnetostructural order in the frustrated spinel $LiInCr_4O_8$. *Phys. Rev. B* **91**, 174435 (2015).

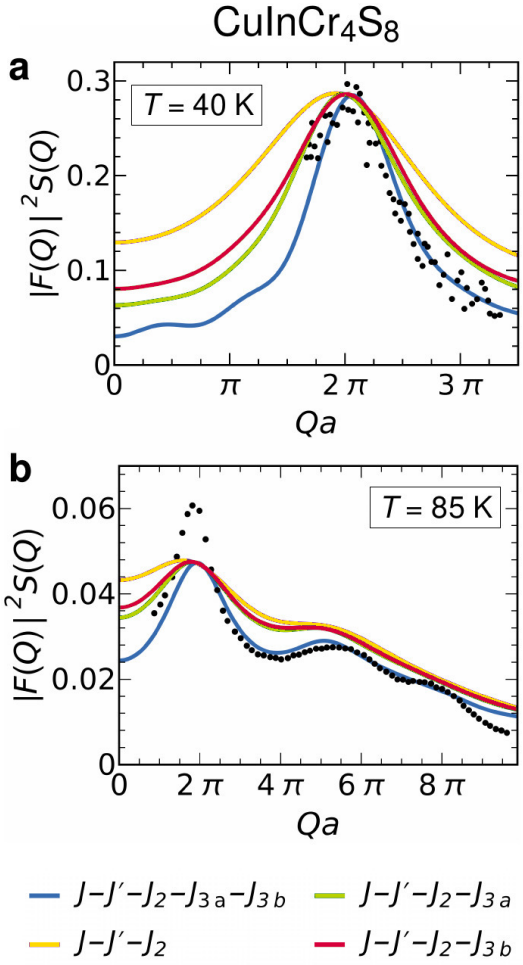

Supplementary Figure 6. **Importance of subleading interactions.** The comparison of $|F(Q)|^2 S(Q)$ for different combinations of J, J', J_2, J_{3a}, J_{3b} with the experimental data obtained by Plumier *et al.*[10] at (**a**) 40K and (**b**) 85K for $CuInCr_4S_8$. The experimental data is shown in black dots. From both the plots, it is very evident that the best match with the experimental data is *only* obtained only with the full J-J'-J_2- J_{3a}-J_{3b} model. This further validates the value of exchange couplings used in our calculations regarding $CuInCr_4S_8$.

[2] Pokharel, G. et al. Negative thermal expansion and magnetoelastic coupling in the breathing pyrochlore lattice material $LiGaCr_4S_8$. *Phys. Rev. B* **97**, 134117 (2018)

[3] Iqbal, Y. et al. Paramagnetism in the kagome compounds $(Zn,Mg,Cd)Cu_3(OH)_6Cl_2$. *Phys. Rev. B* **92**, 220404(R) (2015).

[4] Guterding, D., Valentí, R. & Jeschke, H. O. Reduction of magnetic interlayer coupling in barlowite through isoelectronic substitution. *Phys. Rev. B* **94**, 125136 (2016).

[5] Jaubert, L. D. C. et al. Topological-sector fluctuations and Curie-law crossover in spin ice. *Phys. Rev. X* **3**, 011014 (2013).

[6] Okamoto, Y., Nilsen, G. J., Attfield, J. P. & Hiroi, Z. Breathing pyrochlore lattice realized in A-Site ordered spinel oxides $LiGaCr_4O_8$ and $LiInCr_4O_8$. *Phys. Rev. Lett.* **110**, 097203 (2013).

[7] Okamoto, Y. Magnetic and structural properties of A-site ordered chromium spinel sulfides: Alternating antiferromagnetic and ferromagnetic interactions in the breathing pyrochlore lattice. *J. Phys. Soc. Jpn.* **87**, 034709 (2018).

[8] Yokoyama, H. & Chiba, S. Preparation and magnetic properties of a new selenide spinel $Cu_{1/2}In_{1/2}Cr_2Se_4$. *J. Phys. Soc. Jpn.* **27**, 505 (1969).

[9] Plumier, R., Lotgering F. K. & van Stapele, R. P. Magnetic properties of $Cu_{1/2}In_{1/2}Cr_2S_4$ and some related compounds. *J. Phys. Colloques* **32**, C-1 324-C-1 325 (1971).

[10] Plumier, R. Sougi, M. & Lecomte, M. Observation of an unusual short range magnetic ordering in spinel $Cu_{1/2}In_{1/2}Cr_2S_4$. *Phys. Lett.* **60A**, 341-344 (1977).

[11] Pinch, H. L., Woods, M. J. & Lopatin, E. Some new mixed A-site chromium chalcogenide spinels. *Mat. Res. Bull.* **5**, 425-430 (1970).

[12] Sears, V. F. Neutron scattering lengths and cross sections. *Neutron News* **3**, 26-37 (1992).

[13] Benton, O. & Shannon, N. Ground state selection and spin-liquid behaviour in the classical Heisenberg model on the breathing pyrochlore lattice. *J. Phys. Soc. Jpn.* **84**, 104710 (2015).

[14] Luttinger, J. M. & Tisza, L. Theory of dipole interaction in crystals. *Phys. Rev.* **70**, 954-964 (1946).

[15] Kaplan, T. A. & Menyuk, N. Spin ordering in three-dimensional crystals with strong competing exchange interactions. *Phil. Mag.* **87**, 3711-3785 (2007).

[16] Lapa, M. F. & Henley, C. L. Ground states of the classical antiferromagnet on the pyrochlore lattice. Preprint at https://arxiv.org/abs/1210.6810 (2012).

[17] Duda, H. et al. Spin-glass-like behavior in single-crystalline $Cu_{0.44}In_{0.48}Cr_{1.95}Se_4$. *Phys. Rev. B* **77**, 035207 (2008).

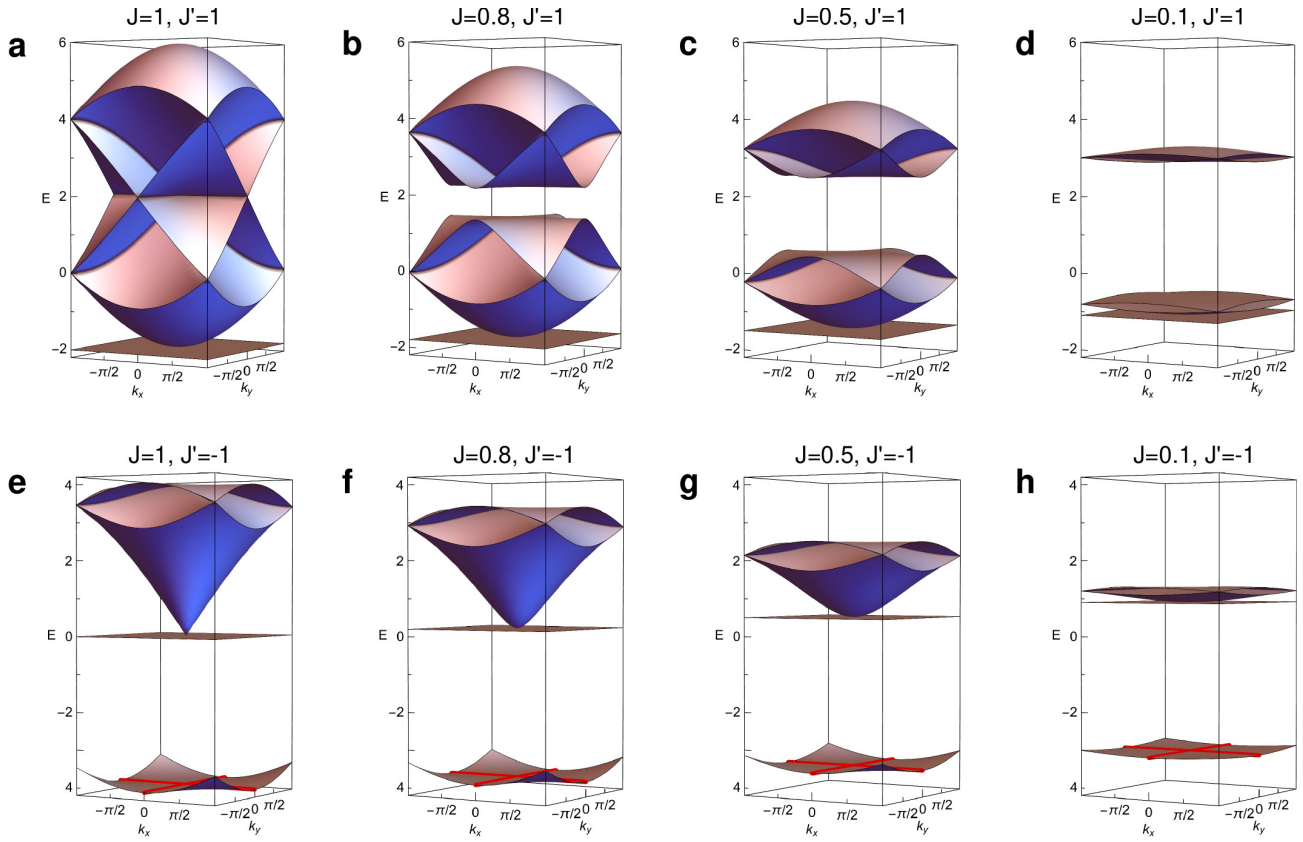

Supplementary Figure 7. **Luttinger-Tisza results.** Eigenvalues of the Luttinger-Tisza matrix for the breathing pyrochlore Hamiltonian with nearest-neighbor exchanges J and J'. **a-d** Antiferromagnetic case for constant $J' = 1$ and decreasing J. **e-h** Ferromagnetic $J' = -1$ with decreasing antiferromagnetic J. All plots show the $(h, k, 0)$ plane, with k_z chosen to be zero.

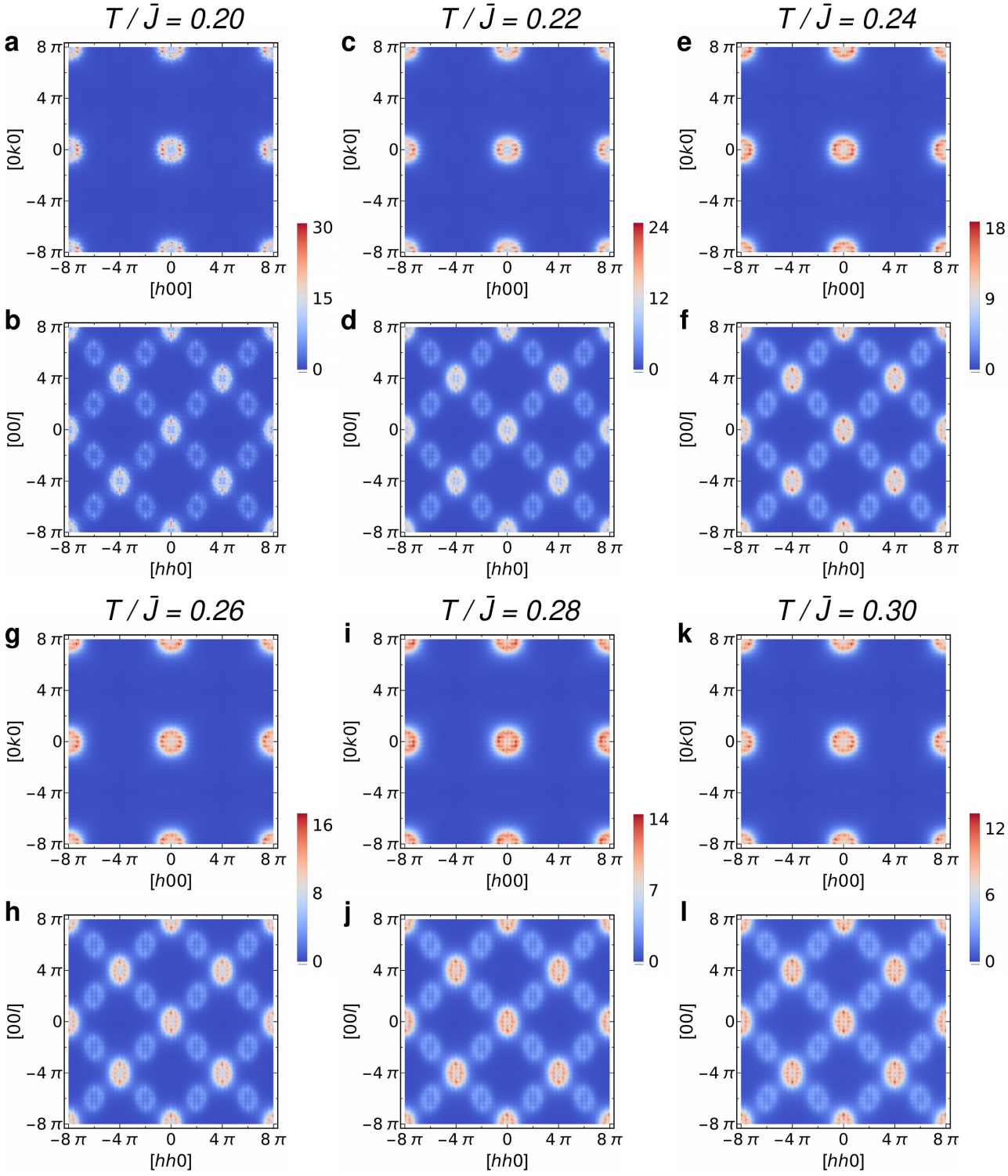

Supplementary Figure 8. **Classical Monte Carlo results.** The spin (not neutron) structure factor for $CuInCr_4Se_8$ obtained using classical Monte Carlo simulations (system of $32 \times 32 \times 32 \times 16 = 524288$ spins) projected on $[hk0]$ (first row) and $[hhl]$ (second row) planes. Susceptibility units are $1/\bar{J}$ ($\bar{J} = \sqrt{J^2 + J'^2}$). At the ordering temperature $T/\bar{J} = 0.20$, the Bragg peaks at $\mathbf{q} = (0.40 \pm 0.04)$ are clearly visible, however, at progressively higher temperatures the spectral weight gradually becomes more uniformly distributed leading to the appearance of an approximate spiral spin liquid. The axes are in units of $1/a$, $a = 10.5735$ Å[17].